Microstructure Evolution During Post-heat Treatment of Haynes 282 Alloy Processed by Wire-Arc Additive Manufacturing

Luis Fernando Ladinos Pizano, Soumya Sridar, Chantal Sudbrack, and Wei Xiong

Abstract Post-heat treatment optimization is imperative to improve the mechanical properties of superalloys prepared by additive manufacturing. In this work, the effect of solution treatment on the microstructural heterogeneity and γ' precipitation of Haynes 282 fabricated by wire-arc additive manufacturing (WAAM) has been investigated. The results suggest that the standard solution treatment carried out at 1150 °C for 2 h is insufficient to remove the grain texture developed during WAAM. Instead, a heat treatment at 1250 °C for 2 h facilitates homogenization and recrystallization without causing excessive coarsening. Furthermore, solution treatment temperature affects the kinetics of γ' precipitate growth. By increasing the solution heat treatment temperature from 1150 to 1250 °C, strengthening γ' precipitates grow faster, achieving the peak hardness earlier. Moreover, the increase in solution temperature favors the development of a bimodal distribution of γ' precipitates during aging. This work demonstrates the need for an effective post-heat treatment to eliminate the heterogeneities that are formed during the WAAM process and alter the γ' size distribution to improve the mechanical performance of Haynes 282 alloy.

Keywords Haynes 282 · Additive manufacturing · CALPHAD · Precipitation behavior · Strengthening mechanism

Introduction

The global energy demand has driven the development of more efficient and ecological power plants. An impactful way to increase thermal efficiency and reduce plant pollution is to increase the operating temperature and pressure of industrial gas turbines used for power generation. However, the turbine operating conditions are

L. F. L. Pizano · S. Sridar · W. Xiong (✉)
Physical Metallurgy and Materials Design Laboratory, Department of Mechanical Engineering and Materials Science, University of Pittsburgh, Pittsburgh, PA 15261, USA
e-mail: weixiong@pitt.edu

C. Sudbrack
National Energy Technology Laboratory, Albany, OR 97321, USA

E. A. Ott et al. (eds.), *Proceedings of the 10th International Symposium on Superalloy 718 and Derivatives*, The Minerals, Metals & Materials Series,
https://doi.org/10.1007/978-3-031-27447-3_46

limited by the mechanical properties of the key structural components, promoting the design of materials with excellent mechanical performance at high temperatures (>760 °C).

Haynes 282 is a precipitation-strengthened nickel-base superalloy with high creep strength along with excellent tensile and fatigue behavior at 760 °C, which has target use in advanced ultra-super-critical (A-USC) turbines [1]. Moreover, Haynes 282 shows good fabricability and weldability as the volume fraction of the reinforcing phase (γ') is relatively low (19%) compared to other commercial nickel-base superalloys. However, a low γ' content in general negatively impacts mechanical properties. To compensate for the low volume fraction of γ', Haynes 282 incorporates a generous amount of Mo, improving mechanical performance through solid solution strengthening [2]. Likewise, γ' precipitates and a distribution of micron-sized MC and $M_{23}C_6$ carbides significantly improve the mechanical behavior of Haynes 282. While γ' improves both tensile properties and creep resistance, MC and $M_{23}C_6$ carbides stabilize the grain structure at high temperatures, favoring creep resistance [3].

The microstructure and mechanical performance of Haynes 282 are optimized by applying a post-heat treatment comprising of solution heat treatment and aging steps. The standard heat treatment developed by Haynes International Inc. consists of a solution treatment above the solvus temperature of γ' and $M_{23}C_6$ carbides, carried out between 1121 °C and 1149 °C. Subsequently, two aging heat treatments at 1010 and 788 °C are recommended to precipitate $M_{23}C_6$ carbides and γ', respectively [4]. The traditional manufacturing processes for Haynes 282 are forging and casting. However, the product forms are limited by the hardness of the material and the ability to create hollow structures such as cooling ducts. Due to the geometric freedom offered by additive manufacturing (AM) and the excellent weldability of Haynes 282, the trend to process Haynes 282 by AM has increased in recent years.

AM is a computer-aided manufacturing technique capable of producing 3D objects from the addition of material layer-by-layer. The versatility of this methodology facilitates the production of customizable components with complex geometries and final finishes. Wire arc additive manufacturing (WAAM) is a direct energy deposition (DED) technique used in the fabrication and repair of metal components with wire as starting material. The solidification process along with the heating and cooling cycles associated with WAAM introduces microstructural variation compared to samples produced by conventional techniques. Therefore, studying the effect of WAAM process conditions and post-heat treatments on the microstructure and mechanical properties is imperative.

Recently, it has been shown that additively manufactured Haynes 282 can match or even exceed the mechanical properties of wrought alloy by modifying the post-heat treatment conditions. Ramakrishnan and Dinda [5] reported that Haynes 282 fabricated by powder-based direct laser metal deposition is able to achieve an ultimate tensile strength of 1200 MPa and ductility of 18% after application of single-step aging heat treatment at 788 °C for 16 h. However, most of the works reported up to now [6] are dedicated exclusively to optimizing the characteristics of γ' precipitates and mechanical properties without considering the heterogeneity associated with the columnar grain structure.

This work focuses on the design of post-heat treatments capable of minimizing grain structure heterogeneity and maximizing the mechanical strength through γ' precipitation in Haynes 282 fabricated using WAAM. The effect of solution heat treatment temperature on grain structure and γ' precipitation during subsequent aging heat treatments has been extensively studied. By elucidating the relationship between solution heat treatment and second aging heat treatment, this paper provides guidance for the design of consecutive post-heat treatments for Haynes 282.

Materials and Methods

Experimental Details

The Haynes 282 sample was fabricated on a stainless steel 304 substrate using the WAAM system GEFERTEC ARC 605 equipped with a Fronius TPS 400i PULSE power source. The diameter of the wire used as feedstock in the WAAM process was 1 mm and its chemical composition as provided by the supplier, Haynes international, USA, is listed in Table 1. The distance from the torch to the substrate was maintained at 14 mm, while the torch travel speed and wire feed rate were 950 mm/min and 6.5 m/min, respectively. An average voltage of 24 V was supplied to the system, producing a current of 140 A. To prevent oxidation of the sample during the manufacturing process, Cronigon Ni10 (mixture of 70% Ar and 30% He) was used as torch shielding gas at a rate of 20 L/min. Furthermore, the scanning strategy consisted of a single bead pattern as shown in Fig. 1. In order to improve the mechanical performance of Haynes 282 samples, the effect of different post-heat treatments on the microstructure and hardness was evaluated. The details of the conditions studied are summarized in Table 2. The heat treatments were performed in a box furnace. To avoid oxidation, the samples were encapsulated in quartz tubes under vacuum and backfilled with Argon.

Microstructure characterization was carried out in the XZ plane along the build direction of the sample as shown in Fig. 1c. The metallographic preparation consisted of a grinding process with SiC abrasive paper followed by a polishing using suspensions of diamond and silica up to a particle size of 0.05 μm. The etchant used to reveal the γ' phase was chromic acid (H_2CrO_4). The characteristics of the precipitates and the grain structure were studied with the scanning electron microscope (SEM, FEI Apreo) operated at 20 kV and equipped with an energy dispersive spectroscope (EDS, EDAX Elite 150) and electron backscatter diffraction (EBSD) detector. Subsequently, the γ' size distribution was calculated by analyzing SEM micrographs with

Table 1 Composition (wt. %) of the Haynes 282 wire used for fabrication of the wall build

Elements	Al	B	C	Co	Cr	Fe	Mn	Mo	Ni	Si	Ti
Composition (wt. %)	1.5	0.005	0.06	10	20	1.5	0.3	8.5	55.8	0.15	2.1

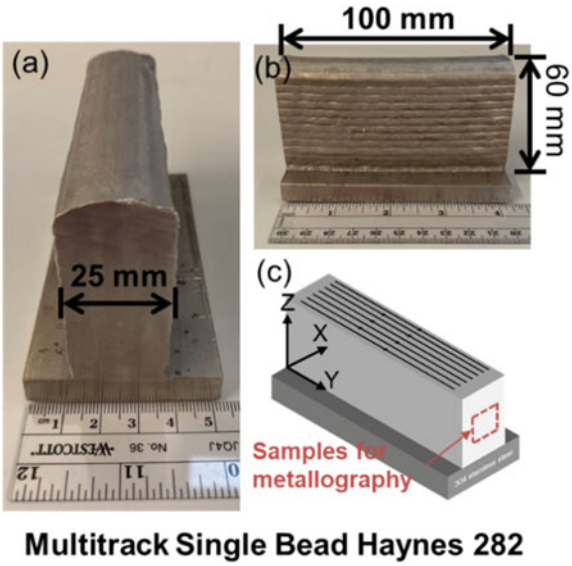

Fig. 1 The thickwall build of WAAM Haynes 282 investigated here in **a** XZ side view and **b** YZ side view with **c** a schematic of the scanning strategy followed during WAAM printing with Z indicating the build direction

Table 2 Conditions and identifications (ID) for all samples studies in this work. After every heat treatment the samples were water quenched

Sample ID	Solution heat treatment	First aging	Second aging
As-built			
ST1150	1150 °C/2 h		
1150-FA	X	1010 °C/2 h	
1150-FA-SA2h	X	X	788 °C/2 h
1150-FA-SA4h	X	X	788 °C/4 h
1150-FA-SA6h	X	X	788 °C/6 h
1150-FA-SA8h	X	X	788 °C/8 h
ST1250	1250 °C/2 h		
1250-FA	X	1010 °C/2 h	
1250-FA-SA2h	X	X	788 °C/2 h
1250-FA-SA4h	X	X	788 °C/4 h
1250-FA-SA6h	X	X	788 °C/6 h
1250-FA-SA8h	X	X	788 °C/8 h

ImageJ software. Microhardness was measured using the LM800-LECO durometer and a Vicker pyramidal indenter. The load and dwell time were 0.3 kg and 10 s, respectively. The average Vickers hardness ($HV_{0.3}$) was determined from 35 indentations separated by 150 μm using 0.3 kg load.

Computational Details

The phase fractions as a function of temperature along with the Scheil solidification diagram and the variation in chemical composition of MC and $M_{23}C_6$ carbides as a function of temperature were predicted using Thermo-Calc software. To perform these thermodynamic calculations, the TCNI11 database developed for Ni-base superalloys together with the chemical composition listed in Table 1 were used.

Results and Discussion

Effect of WAAM Process Conditions on Microstructure

The cooling rate (around 100 °C/s [7]) and the thermal cycles associated with the WAAM process determine the initial microstructures of Haynes 282. SEM images and EDS maps of the secondary phases found in the as-built condition together with the Haynes 282 Scheil solidification diagram are presented in Fig. 2. Ti- and Mo-rich MC primary carbides with irregular morphologies and a size range between 0.30 and 0.45 μm were located in interdendritic regions and Ti-rich nitrides were identified within the γ dendrite core. However, γ′ precipitates were not observed throughout the build.

According to Ojo et al. [8], the solidification process begins with the formation of γ dendrites. As the γ dendrites grow, elements with partition coefficients less than

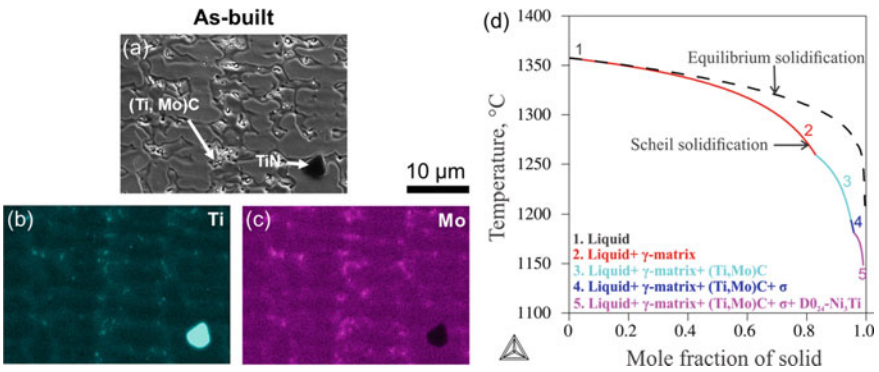

Fig. 2 **a** SEM image of the as-built sample in XZ plane. The dark gray continuous phase represents the γ matrix while the black and light gray precipitates are identified as TiN and (Ti, Mo)C carbides, respectively. Energy dispersive X-ray spectroscopy (EDS) elemental maps, revealing that MC carbides are rich in **b** Ti and **c** Mo. **d** Scheil solidification diagram of Haynes 282, showing the formation of (Ti, Mo)C carbides during the non-equilibrium solidification process

1 such as Ti, Mo, and C begin to segregate into the interdendritic liquid. The liquid continues to be enriched in MC carbides-forming elements until the composition exceeds the maximum solubility of the γ matrix, causing the formation of the non-invariant eutectic γ/MC. This reaction practically consumes the C content of the alloy and is defined as $L \leftrightarrow \gamma + MC$. Subsequently, the interdendritic liquid continues to enrich with γ′-forming alloying elements such as Ti and Al, causing the formation of the eutectic γ/γ′. These reactions explain the presence of (Ti, Mo)C carbides located in interdendritic regions. However, the solidification rates associated with WAAM process prevent the precipitation of γ′. According to the Scheil solidification diagram in Fig. 2d, γ dendrite formation starts at 1360 °C, while the precipitation of γ/MC eutectic takes place at 1260 °C. To decrease the segregation of alloying elements and, therefore, increase the degree of supersaturation in the γ matrix, solution heat treatment followed by water quenching is recommended.

Microstructural Evolution During Solution Heat Treatments

The standard solution heat treatment for wrought Haynes 282 is intended to dissolve secondary phases and reduce residual stresses. However, the solution heat treatment for Haynes 282 fabricated using WAAM should additionally recrystallize the grain structure. The distribution and morphology of the precipitates found in samples ST1150 and ST1250 can be observed from the SEM micrographs shown in Fig. 3. Figure 3a and d shows that MC carbides and their distribution along the interdendritic regions persist after solution heat treatments, which is expected since MC carbides typically have good stability at 1150 °C. However, as the temperature increases, the γ matrix is able to dissolve more alloying elements, causing the size and volume fraction of the MC carbides to decrease in the ST1250 sample.

On the other hand, Fig. 3d and e indicates that the morphology of the MC carbides changes from irregular to blocky as the solution temperature rises from 1150 to 1250 °C and that the dissolution of alloying elements causes the dendritic subgrains to disappear above 1150 °C. Likewise, the MC carbides located at the grain boundaries completely disappeared in the ST1250 sample as shown in Fig. 3f. In general, the dissolution of secondary phases is attributed to the diffusion of atoms across the precipitate/matrix interface into the matrix. The reports by Cieslak et al. [9] and Cao et al. [10] suggest that the dissolution of MC carbides in nickel-based superalloys occurs between 1230 and 1290 °C. These observations explain the presence of MC carbides in the ST1150 and ST1250 samples.

Figure 4 presents the Haynes 282 phase fraction diagram together with the variation in the composition of (Ti, Mo)C carbides as a function of temperature obtained using Thermo-Calc. The diagram in Fig. 4a shows that the fraction of MC carbides decreases from 0.0033 to 0.0013 between 1150 and 1250 °C, which agrees with the experimental observations made from Fig. 3a and d. Likewise, thermodynamic calculations indicate that MC carbides can completely dissolve into the matrix at 1270 °C as suggested by Cieslak et al. [9] and Cao et al. [10]. Figure 4b shows that Ti and Mo

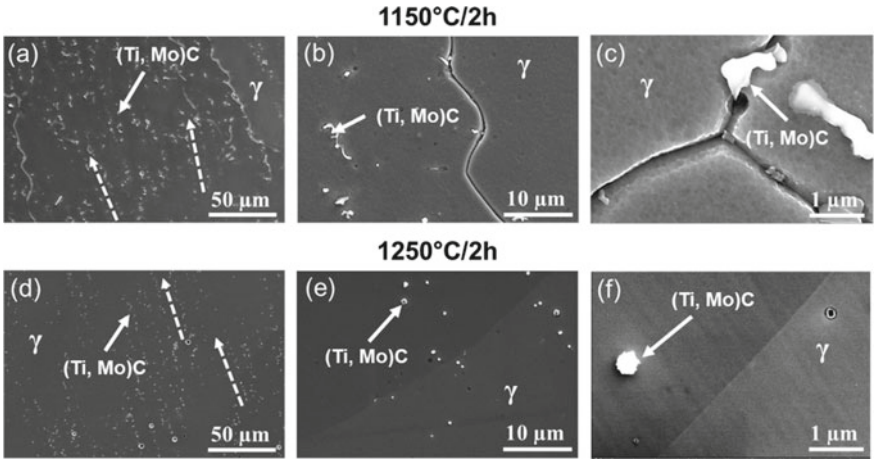

Fig. 3 Distribution and morphology of (Ti, Mo)C carbides as a function of solution temperature, dotted arrows highlight the columnar distribution of precipitates. Distribution of (Ti, Mo)C carbides of **a** ST1150 and **b** ST1250 samples. Carbides with irregular and cubic morphology after solution heat treatment at **c** 1150 °C and **d** 1250 °C, respectively, and **e**, **f** MC carbides located at grain boundaries

are the main constituents of MC carbides, which is consistent with the EDS maps presented in Fig. 2b and c. Furthermore, the solubility of Ti in the carbides reduce as the temperature increases, while the solubility of Mo increases with temperature. The dissolution of (Ti, Mo)C carbides and the reduction of Ti solubility in the remaining carbides at high temperatures increase the degree of supersaturation of the γ matrix in the ST1250 sample, which can improve the precipitation kinetics in the subsequent aging steps.

Figure 5 shows the inverse pole figure (IPF) maps of the as-built, ST1150, and ST1250 samples. According to the IPF maps, the grain structure of the as-built and ST1150 conditions consist of a columnar grain structure, while the ST1250 sample exhibits equiaxed grains and some twin boundaries. Although the directional solidification process of AM tends to introduce texture to the material, the as-built samples did not present strong texture.

The grain morphology is governed by the local direction of heat flow and competitive grain growth during solidification. Wei et al. [11] showed that the grains of nickel-base alloys with FCC matrix grow preferentially when the direction of easy growth <100> is aligned parallel to the direction of maximum heat flux. Wei et al. [12] also suggest that the direction of maximum heat flux in AM is perpendicular to the edge of the molten pool towards the substrate, promoting the formation of columnar structures as observed in the as-built sample.

On the other hand, the epitaxial nucleation and the competitive grain growth define the crystallographic orientation of the grains. According to Li and Tan [13], if the first layer is made up of columnar grains at the base and a large area of equiaxed grains at the top, the subsequent layer will be unable to completely remelt the equiaxed area,

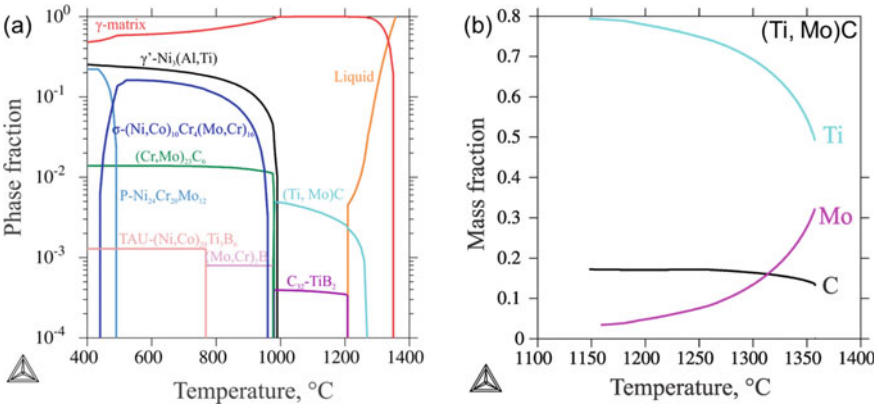

Fig. 4 **a** The phase fraction diagram for Haynes 282 calculated by Thermo-Calc software using TCNI11 database shows that (Ti, Mo)C carbides dissolve in the γ matrix as the temperature increases. **b** The temperature-dependent composition diagram of (Ti, Mo)C carbides indicates that the solubility of Ti in MC carbides decreases with temperature

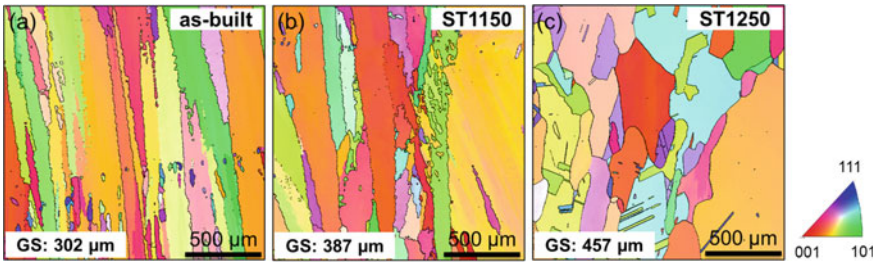

Fig. 5 Inverse pole figure (IPF) maps of the **a** as-built, **b** ST1150, and **c** ST1250 conditions in XZ plane using the FCC γ matrix for indexing

causing new columnar grains to grow epitaxially on equiaxed grains. Consequently, the new columnar grains will adopt the random crystallographic orientations of the equiaxed grains that act as the substrate. As this process introduces new 'competitors,' competitive growth is unable to filter out the most favorable orientations, resulting in a material with no strong texture such as the as-built Haynes 282 sample. As Christofidou et al. [14] and Shaikh et al. [15] reported, the temperature of standard solution heat treatment is not sufficient to recrystallize the grain structure of Haynes 282 processed by AM. However, the results suggest that the heat treatment at 1250 °C for 2 h allowed the sample to completely recrystallize, decreasing the heterogeneity of the grain structure.

Residual stresses and grain size have a significant effect on the mechanical performance of alloys. In general, grain coarsening and residual tensile stresses decrease the mechanical properties. The contribution of the microstructural characteristics on the alloy strength can be carried out through the hardness test. The microhardness

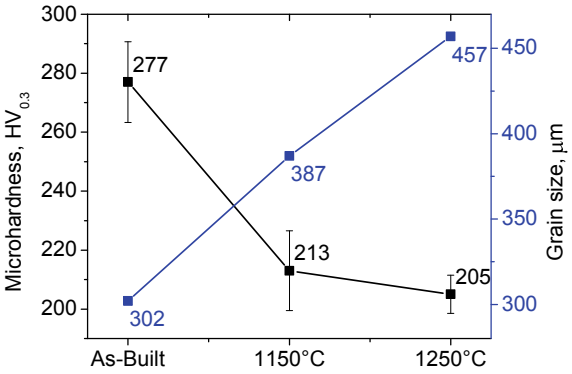

Fig. 6 The microhardness and grain size of Haynes 282 as a function of solution treatment temperature

and grain size of the as-built, ST1150, and ST1250 samples, are shown in Fig. 6. The profiles in this figure indicate that as the solution temperature increases, the microhardness drops and the grain size increases, reaching a value of 205 $HV_{0.3}$ and 457 µm, respectively.

Thermal cycles intrinsic to additive manufacturing cause the material to expand and contract at different rates, increasing the residual stresses and therefore the hardness of the as-built samples. On the other hand, the softening of samples ST1150 and ST1250 is attributed to temperature-assisted recovery and grain coarsening processes. The combined effect of grain growth and relaxation of residual stresses causes the hardness of the ST1150 sample to decrease by 64 $HV_{0.3}$ compared to the as-built sample. However, even though the grain size increases continuously, the hardness of the ST1250 sample decreases by only 8 $HV_{0.3}$ compared to the ST1150 sample. Therefore, the relief of residual stresses is the main cause of the drop in hardness. Similar results have been reported in several works available in the literature [16, 17]. These results suggest that solution heat treatments above 1150 °C are sufficient to relieve the residual stresses developed during the AM process.

Precipitation of $M_{23}C_6$ Carbides Throughout the First Aging

To increase the thermal stability of the grains at high temperatures and thus, the creep resistance, Haynes 282 is aged at 1010 °C for 2 h. This heat treatment is aimed at the formation of Cr- and Mo-rich $M_{23}C_6$ carbides at the grain boundaries. Figure 7 shows an SEM micrograph, EDS maps, and the temperature-dependent chemical composition plot calculated using Thermo-Calc for $(Cr, Mo)_{23}C_6$ carbides found in 1150-FA and 1250-FA samples. Figure 7a indicates that $(Cr, Mo)_{23}C_6$ carbides tend to distribute over grain boundaries, whereas Fig. 7b and c proves that Cr and Mo are the main constituents of this phase, which is corroborated by the computational prediction shown in Fig. 7d.

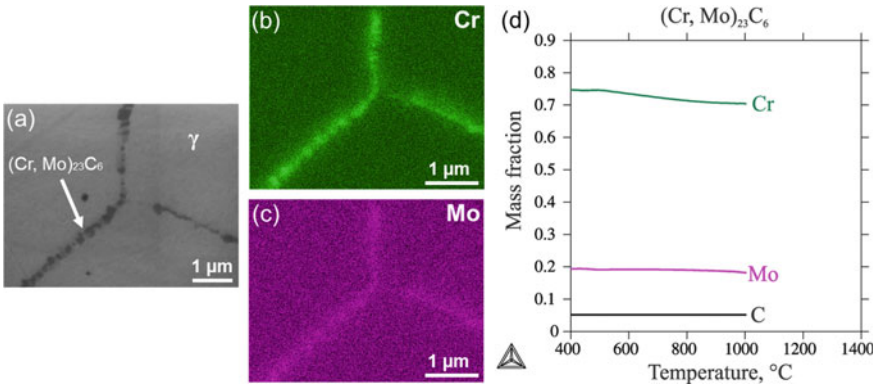

Fig. 7 **a** Representative SEM micrograph of microstructure of the 1150 + FA and 1250 + FA samples, EDS maps of **b** Mo and **c** Cr and **d** the evolution of the chemical composition of the $M_{23}C_6$ carbides as a function of temperature, indicating the presence of Cr and Mo in these precipitates

Unlike the MC-type primary carbides that precipitate during the solidification process in interdendritic regions from the liquid phase due to the segregation of alloying elements, the $M_{23}C_6$-type secondary carbides precipitate from the γ matrix. However, due to the high interfacial energy involved in the formation of the $\gamma/M_{23}C_6$ interface, the $M_{23}C_6$ carbides grow preferentially on the grain boundaries. The work carried out by El-Bagoury [18] suggests that the $M_{23}C_6$ carbides precipitate due to the decomposition of the primary MC carbides at high temperatures or the presence of remaining carbon in the matrix. The reaction between the MC carbides and the matrix results in the formation of $M_{23}C_6$ carbides and γ′ ($MC + \gamma \rightarrow M_{23}C_6 + \gamma'$), or in some cases, it results in the precipitation of M_6C carbides and γ′ ($MC + \gamma \rightarrow M_6C + \gamma'$). According to Adelajda et al. [19], taking into account the chemical composition of Haynes 282, the previous reactions are described as

$$(Ti,\ Mo)C + (Ni,\ Cr,\ Al,\ Ti) \rightarrow Cr_{21}Mo_2C_6 + Ni_3(Al,\ Ti)$$
$$(Ti,\ Mo)C + (Ni,\ Co,\ Al,\ Ti) \rightarrow Mo_3(Ni,\ Co)_3C + Ni_3(Al,\ Ti)$$

On the other hand, Lvov et al. [20] suggest that these reactions are dominated by the diffusion of carbon from the MC carbide to the matrix and the diffusion of Ni, Cr, and Co in the opposite direction. Since the first aging temperature is above the γ′ solvus temperature (997 °C), γ′ phase does not precipitate, and the hardness does not increase significantly after this heat treatment. The hardness of samples 1150-FA and 1250-FA increases around 20 $HV_{0.3}$ compared to samples ST1150 and ST1250, respectively. Therefore, a second aging heat treatment is required to induce γ′ precipitation and improve the mechanical properties.

Effect of Solution Temperature on γ′ Phase Precipitation During Second Aging

The precipitation of γ′ prevents the movement of dislocations through the material, improving the mechanical strength of Haynes 282. However, the improper selection of the aging treatment parameters negatively affects the mechanical behavior of the alloy. High aging temperatures lead to low degrees of undercooling and supersaturation of the γ matrix, hindering the nucleation process, while low temperatures prevent diffusion of the essential alloying elements and therefore γ′ growth. Likewise, long aging times cause over-aging of γ′ precipitates. Therefore, the design of second aging conditions is crucial. According to Kruger [21], the volume fraction and diameter of γ′ in the fully aged condition of Haynes 282 are about 19% and 20 nm, respectively. On the other hand, Shin et al. [3] showed that solution treatment conditions have a profound effect on γ′ precipitation, suggesting that the temperature and time of the second aging should be optimized based on the conditions of the previous solution heat treatment.

The morphology and size distribution of the γ′ phase as a function of solution temperature and second aging time are seen in the SEM micrographs and histograms shown in Figs. 8 and 9, respectively. The SEM micrographs show that the spherical morphology of γ′ remains invariant regardless of solution temperature and aging time, which can be attributed to the 0.2% lattice mismatch between γ and γ′ phases [22]. The histograms indicate that γ′ size increases with the second aging time regardless of the solution temperature. These results are expected since the growth of the γ′ phase is controlled by diffusion, therefore, the γ′ size is proportional to the aging time and temperature. However, the γ′ size increases faster in the samples that were exposed to 1250 °C during the previous solution heat treatment, which is more evident at 2 and 4 h of aging. Likewise, 1250-FA-SA6h and 1250-FA-SA8h samples show a bimodal distribution of the γ′ phase. While the smallest (d1) and largest (d2) diameters of γ′ phase in sample 1250-FA-SA6h are 25 and 53 nm, the particle sizes of sample 1250-FA-SA8h are 30 and 61 nm, respectively.

The difference in γ′ size between samples 1150-FA-SAxh and 1250-FA-SAxh can be explained by the precipitation kinetics. According to Mao [23], the volumetric fraction of γ′ increases with the degree of supersaturation of the matrix prior to the aging heat treatment, facilitating the subsequent coarsening process. As discussed above, MC carbides are partially dissolved during solution treatment at 1250 °C, increasing the degree of supersaturation of the matrix. As a result, the γ′ nucleation and growth kinetics in the 1250-FA-SAxh samples are faster compared to the 1150-FA-SAxh samples, causing the γ′ size of the 1250-FA-SAxh samples to be larger.

On the other hand, γ′ can be divided into three different types: primary γ′, cooling γ′, and aging γ′, which refer to precipitates remaining from previous sub-solvus heat treatments, precipitates formed during quenching, and γ′ particles that form from the aging heat treatment, respectively. Jian [23] showed that γ′ can precipitate during the cooling step of solution heat treatment if the cooling rate is low enough below the solvus temperature of γ′ phase (997 °C). Therefore, low cooling rates

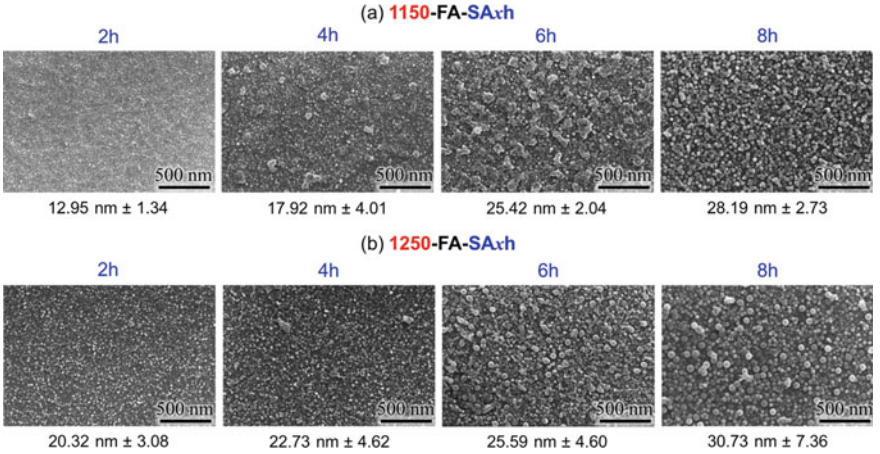

Fig. 8 The precipitation of γ′ during second aging heat treatment carried out at 788 °C for x = 2, 4, 6, and 8 h for samples **a** 1150-FA-SA*x*h and **b** 1250-FA-SA*x*h. The average γ′ diameter is indicated below the metallography of each sample

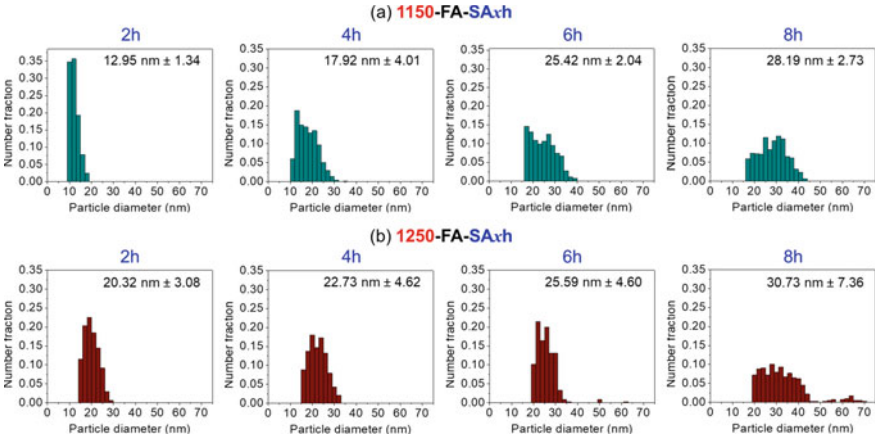

Fig. 9 The histograms of the γ′ size distribution for **a** 1150-FA and **b** 1250-FA samples with different aging heat treatment conditions

and high degrees of matrix supersaturation contribute to the formation of cooling γ′. These observations suggest that although the 1150-FA-SAhx and 1250-FA-SAhx samples were quenched in the same way, the high degree of matrix supersaturation in the 1250-FA-SAhx samples contributes to the formation of cooling γ′ after first-aging heat treatment, leading to a bimodal distribution of γ′ precipitates after the second aging heat treatment. The bimodal distribution is clearer in samples 1250-FA-SA6h and 1250-FA-SA8h since the coarsening of γ′ highlights the difference in size between cooling γ′ and aging γ′.

The mechanical behavior of Haynes 282 is mainly controlled by the size distribution and volume fraction of γ'. If the precipitates are significantly smaller than the length of the dislocation line, the dislocations tend to overcome the precipitate by shearing. On the other hand, if the material is overaged, the dislocations pass the precipitates by looping, resulting in a drop in mechanical strength [24].

Hardness evaluation can be used as a rapid screening mechanism to measure the effect of γ' on the mechanical strength of materials. Figure 10 shows the hardness of 1150-FA-SAxh and 1250-FA-SAxh samples, highlighting the contribution of aging heat treatments. In general, it is observed that the hardness of 1150-FA-SAxh samples (Fig. 10a) are higher than the corresponding 1250-FA-SAxh samples (Fig. 10b). According to these results, high solution heat treatment temperature favors the softening of the material. On the other hand, the precipitation of $M_{23}C_6$ carbides during the first aging has a similar effect on hardness regardless of the previous solution treatment condition.

Furthermore, the maximum hardness of the 1150-FA-SAxh samples (390 $HV_{0.3}$) is reached after 8 h of aging at 788 °C when the γ' diameter is 28 nm, while the peak hardness of the 1250-FA-SAxh samples (374 $HV_{0.3}$) is observed at 6 h when the γ' diameter is 25 nm. The degree of supersaturation of the matrix after the solution heat treatment at 1250 °C causes the peak hardness and the overaged state of the ST1250-FA-SAxh samples to be reached faster compared to the 1150-FA-SAxh samples, resulting in the drop in hardness of 1250-FA-SA8h sample. Adelajda et al. [19] reported that the hardness of forged Haynes 282 after standard two-step aging heat treatment is 373 $HV_{0.3}$, showing that the hardness of Haynes 282 samples manufactured by WAAM are comparable. Interestingly, the contribution of γ' precipitates to the hardness of samples 1150-FA-SA2h and 1250-FA-SA2h is similar despite the difference in particle size being 7.32 nm. However, as the size of the γ' increases, the changes in hardness become more significant. Samples 1150-FA-SA4h and 1250-FA-SA4h indicate that a 4.81 nm change in γ' size produces a hardness variation of 16 $HV_{0.3}$. The results of this work demonstrate that to maximize the hardness

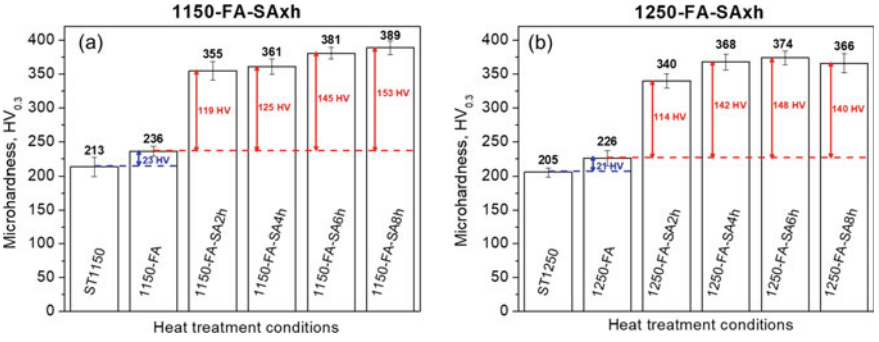

Fig. 10 The effect of heat treatments on the microhardness of Haynes 282 samples heat treated at **a** 1150 and **b** 1250 °C

of Haynes 282, the second aging heat treatment must be optimized based on the conditions of the previous solution heat treatment.

Conclusions

This work is focused on evaluating the effect of different heat treatments on the microstructure and hardness of Haynes 282 deposited using WAAM. The important outcomes of this investigation are as follows.

- The redistribution of alloying elements during the WAAM process allowed the precipitation of MC (M = Ti and Mo) carbides in interdendritic regions. However, the high cooling rate during solidification suppressed the precipitation of γ' phase and $M_{23}C_6$ carbides.
- Solution treatment at 1150 °C eliminated the segregation of alloying elements in interdendritic regions, dissolving the dendritic subgrains observed in the as-built sample. However, the temperature was insufficient to dissolve the primary (Ti, Mo)C carbides. Nevertheless, the volume fraction of (Ti, Mo)C carbides decreased, and the grain structure recrystallized only with solution heat treatment at 1250 °C.
- The first aging heat treatment carried out at 1010 °C promoted the formation of $(Cr, Mo)_{23}C_6$ secondary carbides at grain boundaries without affecting (Ti, Mo)C carbide distribution. The temperature of the solution heat treatment had no noticeable effect on the contribution of the $M_{23}C_6$ carbides to hardness.
- The solution heat treatment temperature has an important effect on the precipitation kinetics of the γ' phase. The degree of supersaturation of the matrix increases with the solution treatment temperature, enhancing the γ' growth rate. Likewise, samples exposed to 1250 °C during solution treatment show a bimodal γ' distribution.
- The hardness profiles show that the peak hardness associated with the γ' precipitation during the second aging was reached faster as the temperature of the previous solution treatment increases. The samples with solution treatment at 1150 °C reached their maximum value at 8 h while the samples exposed to 1250 °C reached the peak hardness at 6 h of the second aging heat treatment.
- The mechanical properties should be determined as future work to comprehensively understand the impact of solution treatments on the structure–property relationship.

Acknowledgements This project is supported via a subcontract from the Pennsylvania State University from the National Energy Technology Laboratory, U. S. Department of Energy, under the University Coalition for Fossil Energy Research program with grant No. DE-FE0026825. The authors would like to appreciate many valuable discussions with Drs. Ping Wang, Bingtao Li, and Jeremy Caron at the Haynes International, Inc. In addition, the authors are grateful for the technical support on printing from GEFERTEC GmbH.

References

1. Shingledecker J, Purgert R, Rawls P (2013) Current status of the U.S. DOE/OCDO A-USC materials technology research and development program, Advances in Materials Technology for Fossil Power Plants: Proceedings from the Seventh International Conference, 41–52.
2. Pike LM (2008) Development of a fabricable gamma-prime (γ') strengthened superalloy. Superalloys 2008, 191–200. https://doi.org/10.7449/2008/Superalloys_2008_191_200.
3. Shin KY, Kim JH, Terner M, Kong BO, Hong HU (2019) Effects of heat treatment on the microstructure evolution and the high-temperature tensile properties of Haynes 282 superalloy. Mater. Sci. Eng. A. 751:311–322. https://doi.org/10.1016/j.msea.2019.02.054.
4. Haynes® 282® alloy Principal Features (2021) Haynes International. https://haynesintl.com/docs/default-source/pdfs/new-alloy-brochures/high-temperature-alloys/brochures/282-brochure.pdf?sfvrsn=20. Accessed 14 September 2022.
5. Ramakrishnan A, Dinda GP (2019) Microstructure and mechanical properties of direct laser metal deposited Haynes 282 superalloy. Mater. Sci. Eng. A. 748:347–356. https://doi.org/10.1016/j.msea.2019.01.101.
6. Ghiaasiaan R, Ahmad N, Gradl PR, Shao S, Shamsaei N (2022) Additively manufactured Haynes 282: effect of unimodal vs. bimodal γ'- microstructure on mechanical properties. Mater. Sci. Eng. A. 831:14234. https://doi.org/10.1016/j.msea.2021.142234.
7. S. Gudur, V. Nagallapati, S. Pawar, G. Mavvala, S. Simhambhatla (2021) A study on the effect of substrate heating and cooling on bead geometry in wire arc additive manufacturing and its correlation with cooling rate. Mater Today Procee. 41:431–436. https://doi.org/10.1016/j.matpr.2020.10.071.
8. Ojo OA, Richards NL, Chaturvedi MC (2006) Study of the Fusion Zone and Heat-Affected Zone Microstructures in Tungsten Inert Gas-Welded inconel 738LC Superalloy. Metall Mater Trans A. 37:421–433. https://doi.org/10.1007/s11661-006-0013-2.
9. Cieslak MJ, Knorovsky GA, Headley Jr. TJ, Romig AD (1989) The Solidification Metallurgy of Alloy 718 and Other Nb-Containing Superalloys, International Symposium on Alloy 718 Metallurgy and Applications, 1–6. https://doi.org/10.7449/1989/Superalloys_1989_59_68.
10. Cao WD, Kennedy RL, Willis MP (1991) Differential thermal analysis (DTA) study of the homogenization process in alloy 718. Superalloys 718, 625 and Various Derivatives, 147–160.
11. Wei HL, Mazumder J, DebRoy T (2015) Evolution of solidification texture during additive manufacturing. Sci Rep. 5: 1–7. https://doi.org/10.1038/srep16446.
12. Wei HJ, Mukherjee T, Debroy T (2016) Grain growth modeling for additive manufacturing of nickel based superalloys. Proceedings of the 6th International Conference on Recrystallization and Grain Growth (ReX&GG) 2016, 265–269. https://doi.org/10.1007/978-3-319-48770-0_39.
13. Li X, Tan W (2018) Numerical investigation of effects of nucleation mechanisms on grain structure in metal additive manufacturing. Comput Mater Sci. 153:159–169. https://doi.org/10.1016/j.commatsci.2018.06.019.

14. Christofidou KA, Pang HT, Li W, Pardhi Y, Jones CN, Jones NG, Stone HJ (2020) Microstructural Control and Optimization of Haynes 282 Manufactured Through Laser Powder Bed Fusion, Superalloys 2020, 1014–1023. https://doi.org/10.1007/978-3-030-51834-9_99.
15. Shaikh AS, Schulz F, Minet-Lallemand K, Hryha E (2021) Microstructure and mechanical properties of Haynes 282 superalloy produced by laser powder bed fusion. Mater Today Commun. 26:102038. https://doi.org/10.1016/j.mtcomm.2021.102038.
16. Huang W, Yang J, Yang H, Jing G, Wang Z, Zeng X (2019) Heat treatment of Inconel 718 produced by selective laser melting: Microstructure and mechanical properties. Mater. Sci. Eng. A. 750:98–107. https://doi.org/10.1016/j.msea.2019.02.046.
17. Fayed EM, Shahriari D, Saadati M, Brailovski V, Jahazi M, Medraj M (2020) Influence of homogenization and solution treatments time on the microstructure and hardness of Inconel 718 fabricated by laser powder bed fusion process. Materials. 13:2574. https://doi.org/10.3390/ma13112574.
18. El-Bagoury N (2016) Ni based superalloy: casting technology, metallurgy, development, properties and applications. Int J Eng Sci Res Technol. 5:108–152.
19. Polkowska A, Polkowski W, Warmuzek M, Cieśla N, Włoch G, Zasada D, Purgert RM (2019) Microstructure and Hardness Evolution in Haynes 282 Nickel-Based Superalloy During Multivariant Aging Heat Treatment. J Mater Eng Perform. 28:3844–3851. https://doi.org/10.1007/s11665-019-3886-0.
20. Lvov G, Levit VI, Kaufman MJ (2004) Mechanism of Primary MC Carbide Decomposition in Ni-Base Superalloys. Metall Mater Trans A. 35:1669–1679. https://doi.org/10.1007/s11661-004-0076-x.
21. Kruger KL (2017) Haynes 282 alloy, in: Augusto Di Gianfrancesco (ed) Materials for Ultra-Supercritical and Advanced Ultra-Supercritical Power Plants, Woodhead Publishing, p 511–545. https://doi.org/10.1016/B978-0-08-100552-1.00015-4.
22. Geddes B, Leon H, Huang X (2010) Superalloys : alloying and performance., ASM International, Ohio, USA.
23. Mao J (2002) Gamma prime precipitation modeling and strength responses in Gamma prime precipitation modeling and strength responses in powder metallurgy superalloys powder metallurgy superalloys, West Virginia University. https://researchrepository.wvu.edu/etd.
24. Adlakha I, Garg P, Solanki KN (2019) Revealing the atomistic nature of dislocation-precipitate interactions in Al-Cu alloys. J Alloys Compd. 797:325–333. https://doi.org/10.1016/j.jallcom.2019.05.110.